Science Advances
AAAS

advances.sciencemag.org/cgi/content/full/6/19/eaaw1838/DC1

Supplementary Materials for

The emergence of heat and humidity too severe for human tolerance

Colin Raymond*, Tom Matthews, Radley M. Horton

*Corresponding author. Email: colin.raymond@jpl.nasa.gov

Published 8 May 2020, *Sci. Adv.* **6**, eaaw1838 (2020)
DOI: 10.1126/sciadv.aaw1838

This PDF file includes:

Text S1. Commentary on Validation of Observed Extreme TW.

To assess the physical realism of the conclusion that TW has already exceeded 35°C at several of the HadISD stations, we focus on the Persian Gulf, whose waters and near-surface atmosphere are sampled independently and frequently by marine traffic and observing platforms, and which is surrounded by the world's largest concentration of extreme TW values measured on land (i.e. >=31°C) (Figs. 1, 4). We scrutinize these additional datasets for evidence of maritime air masses with TW exceeding 35°C, before evaluating whether it is likely that advection from the Persian Gulf can explain the short-lived spikes in TW recorded at the coastal HadISD stations. The presumably more complex processes associated with TW at inland locations such as the Indus River Valley are deserving of a separate study; here, we are constrained to note the qualitative agreement among HadISD, ERA-Interim, and ERA5 *(41)* that the central Indus River Valley is a TW hotspot, and it is particularly interesting in this regard that the higher-resolution ERA5 improves upon ERA-Interim by about 3.5°C on the most extreme days there, versus the approximately 2.0°C improvement in the southern Persian Gulf (Fig. S4).

Hourly, point-scale measurements of atmosphere-ocean conditions in the Persian Gulf are taken from the International Comprehensive Ocean-Atmosphere Data Set (ICOADS) *(39)*, which contains 64,734 observations of TW, dewpoint and SSTs reported by ships, buoys, and other observing platforms in the region 23-31°N, 46-57°N between June-September, 1979-2017. Over this period ICOADS registers 312 observations (0.95% of available measurements) with TW exceeding 35°C, and 4,647 SST observations (9.5% of available measurements) above 35°C. Over the Persian Gulf, the fraction of both SSTs and TW above 35°C peaked in 2017, reaching 32.6% and 5.9% of July-September observations, respectively (Fig. S16). Evidently, these marine observations independently suggest that TW ≥35°C has already been observed, and there is good physical consistency with the co-located SSTs which also regularly exceed this threshold. The ERA-Interim reanalysis supports the notion that the globally highest TW values occur over the Persian Gulf waters rather than over the adjacent land (Figs. 4, S10, S17).

To assess whether advection of air masses from the Persian Gulf could then explain the rapid increases in humidity in TW at nearby HadISD stations, we investigate circulation during extreme TW events using the Integrated Global Radiosonde Archive *(22,39)*. Radiosonde humidity data are reliable in the lower troposphere, and if anything have a slight dry bias there *(42)* — where radiosondes (and consequently 4D gridded products) are known to exhibit humidity biases is in very cold or dry conditions (hence not relevant here), and especially prior to 2000 *(43,44)*. For radiosonde stations in the coastal Persian Gulf area, we find consistency of values with the HadISD stations (Figs. S6-S8), and also that wind directions for the highest TW values are generally quite different from those for less-extreme values (Figs. S6-S8), a shift that is tightly confined to the lowest part of the planetary boundary layer. In contrast, stations in North America (represented by Dulles Airport, Virginia) exhibit no such vertical confinement nor a wind shift between moderate and extreme TW values (Fig. S9). These anomalous onshore winds at low levels can be seen in Fig. S3 for Ras al-Khaimah, UAE and in Figs. S6-S8 for Abu Dhabi, UAE; Muscat, Oman; and Bandar Abbas, Iran (the only stations around the Persian Gulf with sufficient radiosonde data to evaluate circulation at times with TW above its 99.75th percentile). The winds cause advection of marine air which we suggest may be driving the observed sharp peaks in TW (Fig. S5). It is also noteworthy that ERA-Interim resolves these

winds quite poorly compared to the 2x-better-resolution ERA5 (Fig. S3), and similarly for winds channeled by topography in the Indus River Valley (Fig. S4), suggesting that further model developments and resolution improvements could lead to additional increases in the accuracy of representing peak TW.

Finally, we consider most broadly the reliability of all of our quality-controlled HadISD stations that have recorded TW >= 33°C at least 5 times (Fig. S18). This illustrates the overall temporal consistency of dewpoint extremes at each station, as well as the similarity of values among stations in the coastal Middle East. Fig. S19 then shows similarities across the world in the amount by which the all-time maximum TW (Fig. S1) exceeds the much-more-readily-validated 95th percentile of TW. Table S1 underscores the large number of 33ºC days, their geographic diversity, and also the fact that the full distribution of TW provides a clearer sense of how a TW of 33ºC typically requires only modest positive anomalies of heat and humidity. In presenting boxplots of all TW recordings by month, Fig. S20 makes a similar argument for the two stations with the most TW=35ºC readings (Ras Al-Khaimah, UAE, and Jacobabad, Pakistan).

Our final dataset reflects a thorough re-examination of the HadISD dataset using both algorithmic and manual analyses, and we believe that our efforts represent a fair balance between eliminating stations or individual days with any potentially questionable aspects, while retaining true anomalies explicable by the physical processes described above.

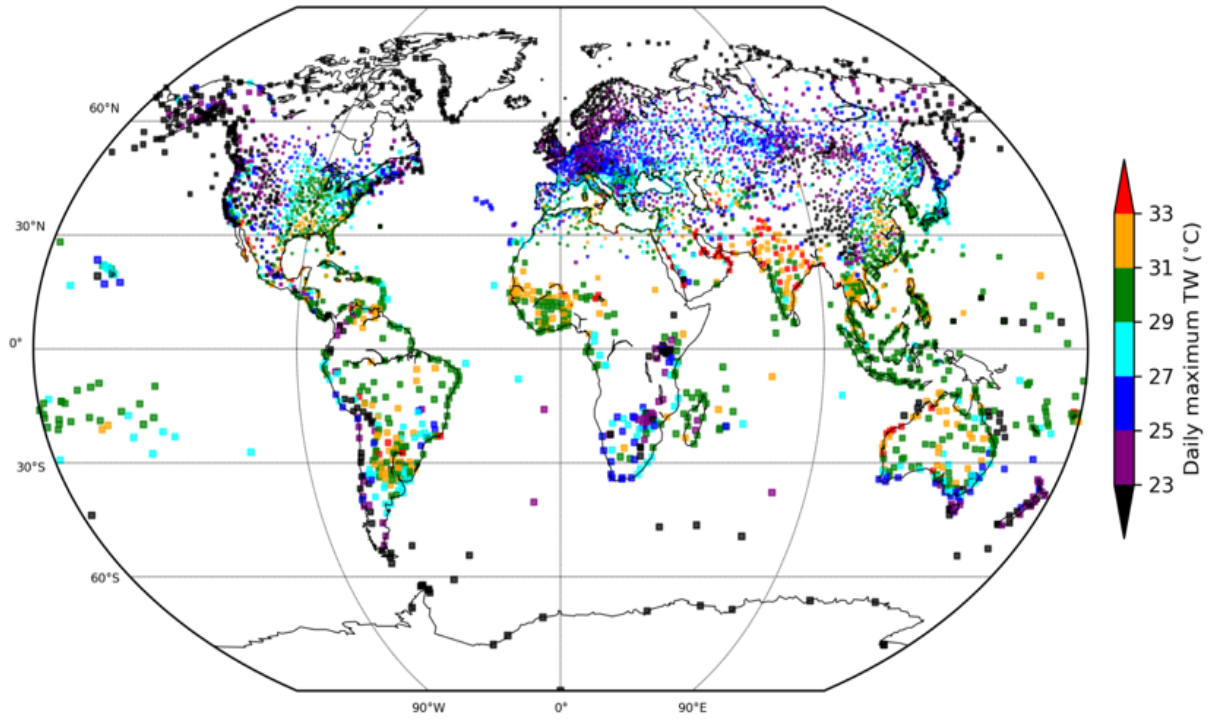

Figure S1. All-time maximum observed extreme humid heat at weather stations. The all-time maximum of TW in HadISD for 1979-2017, for stations with at least 50% data availability over this period. Note that marker size is inversely proportional to station density.

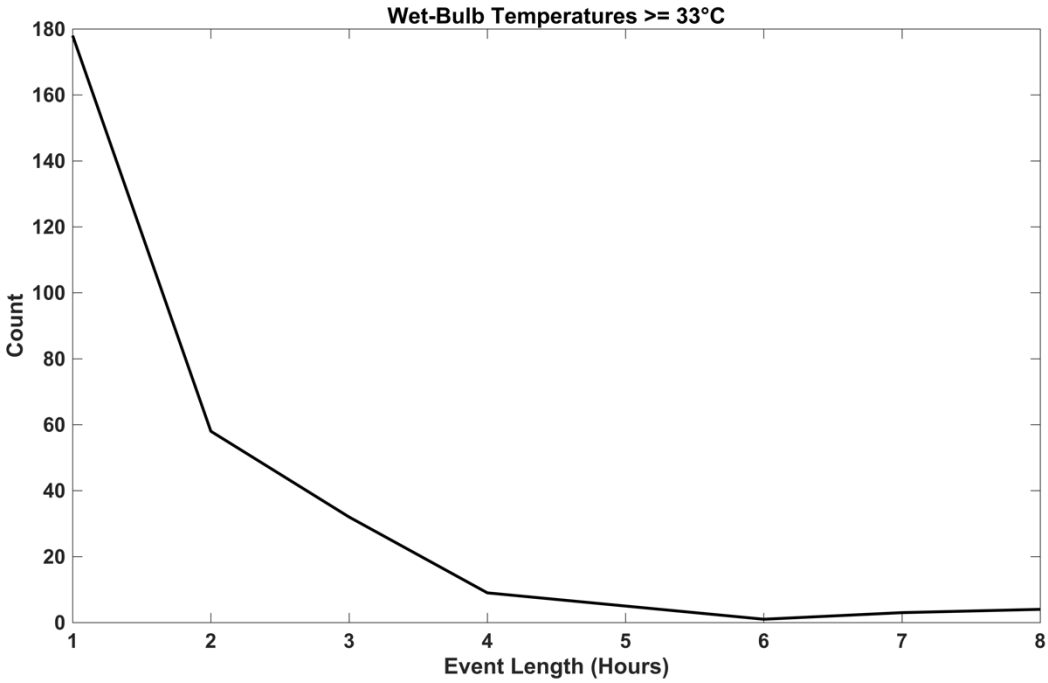

Figure S2. Brevity of observed extreme humid heat at weather stations. Event lengths for all instances in HadISD of TW>=33°C, considering only the *n*=21 stations with regular hourly data on days when TW>=33°C is observed.

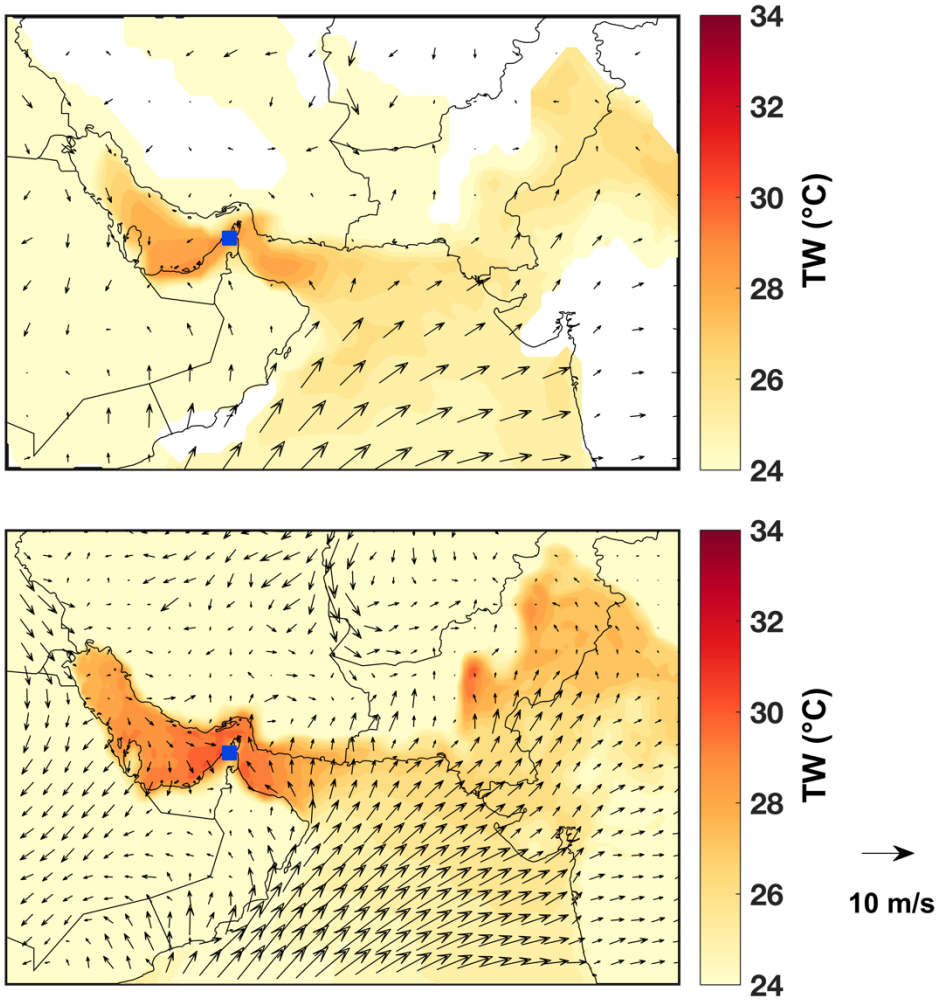

Figure S3. Meteorological conditions when TW=35°C. (Top) ERA-Interim composite of 10-m winds and 2-m TW on the n=4 days when TW=35°C was recorded at Ras al-Khaimah, UAE (blue square). Resolution of plotted data is 0.5°x0.5° and 6-hourly. (Bottom) Same as top but for ERA5. Resolution of plotted data is 0.25°x0.25° and 1-hourly. Mean TW daily maximum near station location is 28.7°C for ERA-Interim and 30.8°C for ERA5.

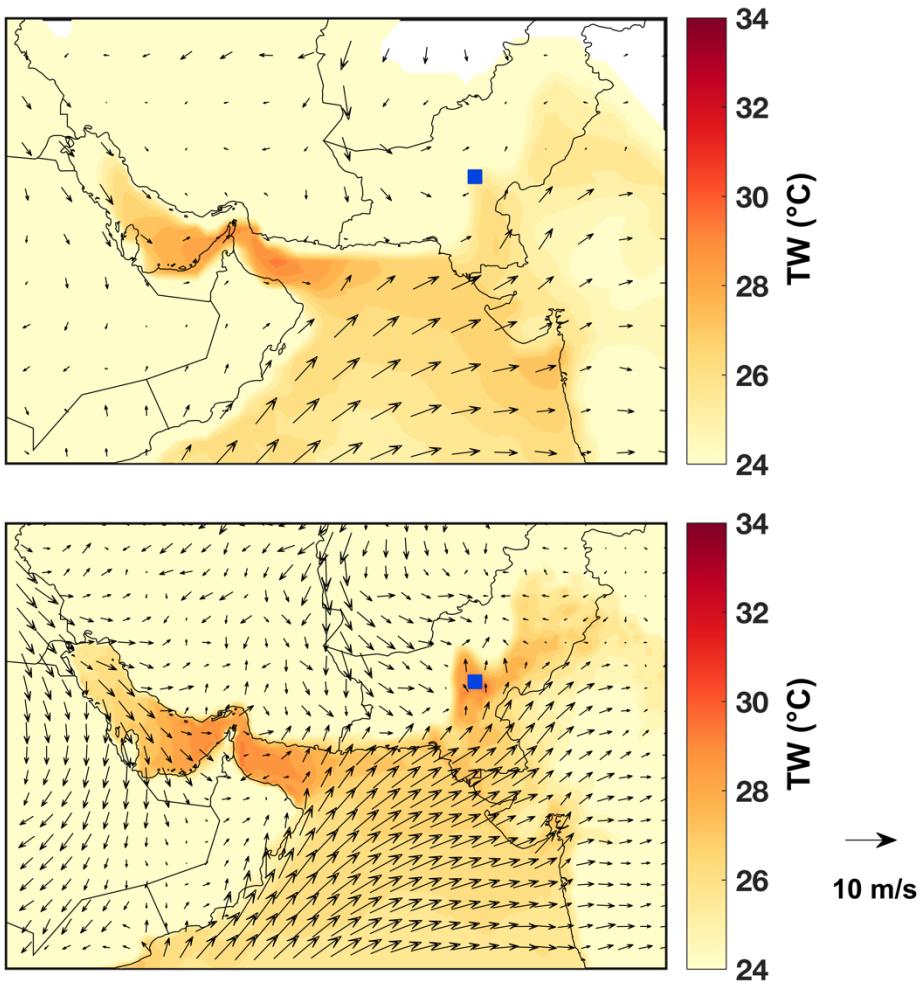

Figure S4. Meteorological conditions when TW=35°C. Same as Figure S3 but for Jacobabad, Pakistan (n=6). Mean TW daily maximum near station location is 26.7°C for ERA-Interim and 30.3°C for ERA5.

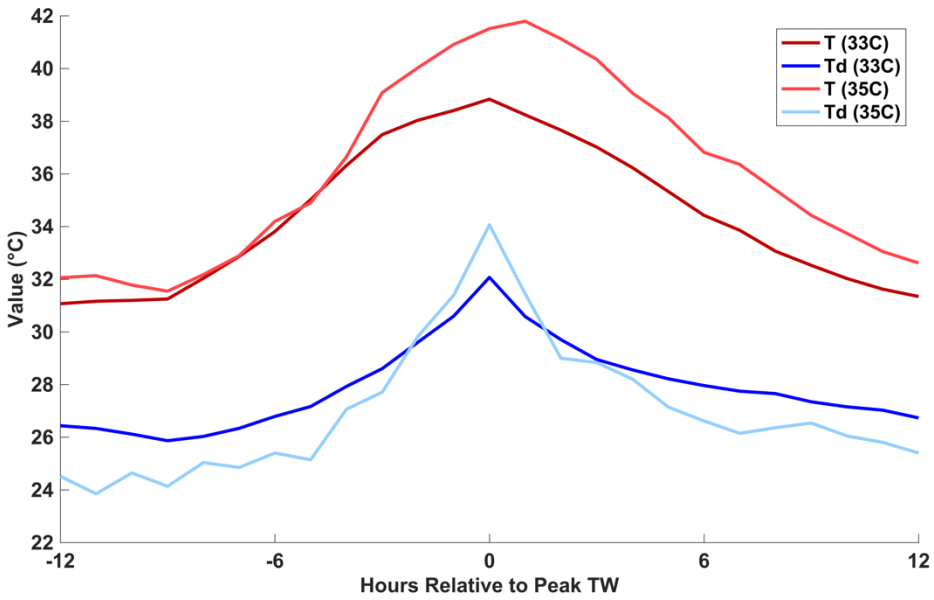

Figure S5. Hourly dry-bulb and dewpoint temperatures for the most extreme wet-bulb temperature days. Mean dry-bulb temperature (red) and dewpoint temperature (blue) in the 12 hours surrounding all 213 TW=33°C and 14 TW=35°C occurrences with available hourly data from HadISD.

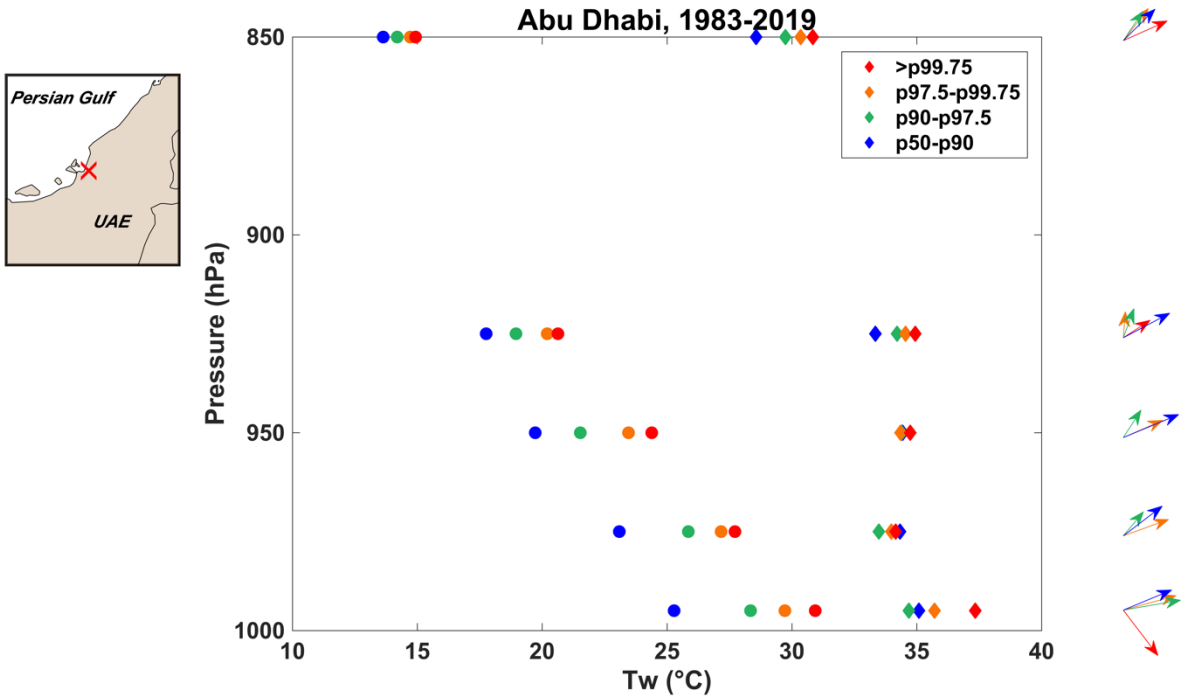

Figure S6. Vertical profiles of coastal extreme humid heat. Radiosonde temperature (diamonds) and TW (circles) for Abu Dhabi International Airport, United Arab Emirates at 12Z on all days between 1983 and 2019 with a lowest-level TW value greater than the annual 99.75th percentile (red, 10 days); between the annual 97.5th and 99.75th percentiles (orange, 90 days); between the annual 90th and 97.5th percentiles (green, 298 days); and between the annual 50th and 90th percentiles (blue, 1593 days). Profiles are truncated at 850 hPa for visibility. Vectors on the right-hand side indicate composite wind speed and direction on these days for each height bin, where available; the map on the left-hand side is a 2.5ºx2.5º box indicating the location of the launch site.

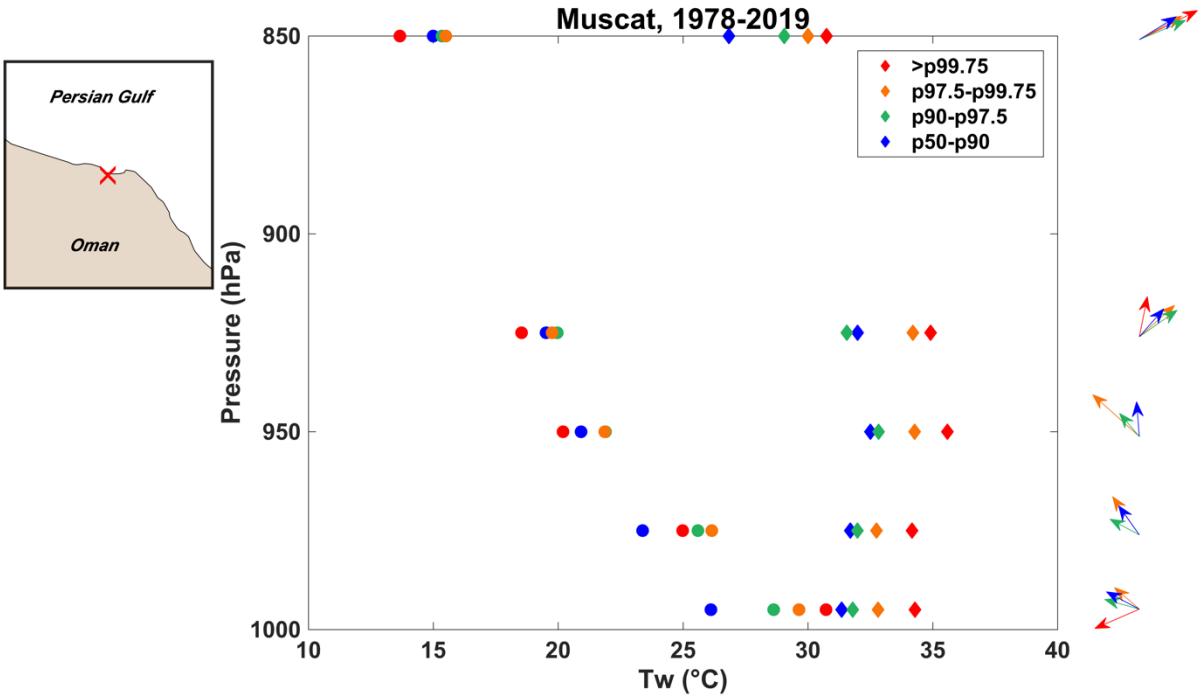

Figure S7. Vertical profiles of coastal extreme humid heat. Same as Figure S6 but for Muscat, Oman. Here, TW values greater than the annual 99.75th percentile comprise 10 days; those between the annual 97.5th and 99.75th percentiles, 88 days; those between the annual 90th and 97.5th percentiles, 288 days; and those between the annual 50th and 90th percentiles, 1546 days.

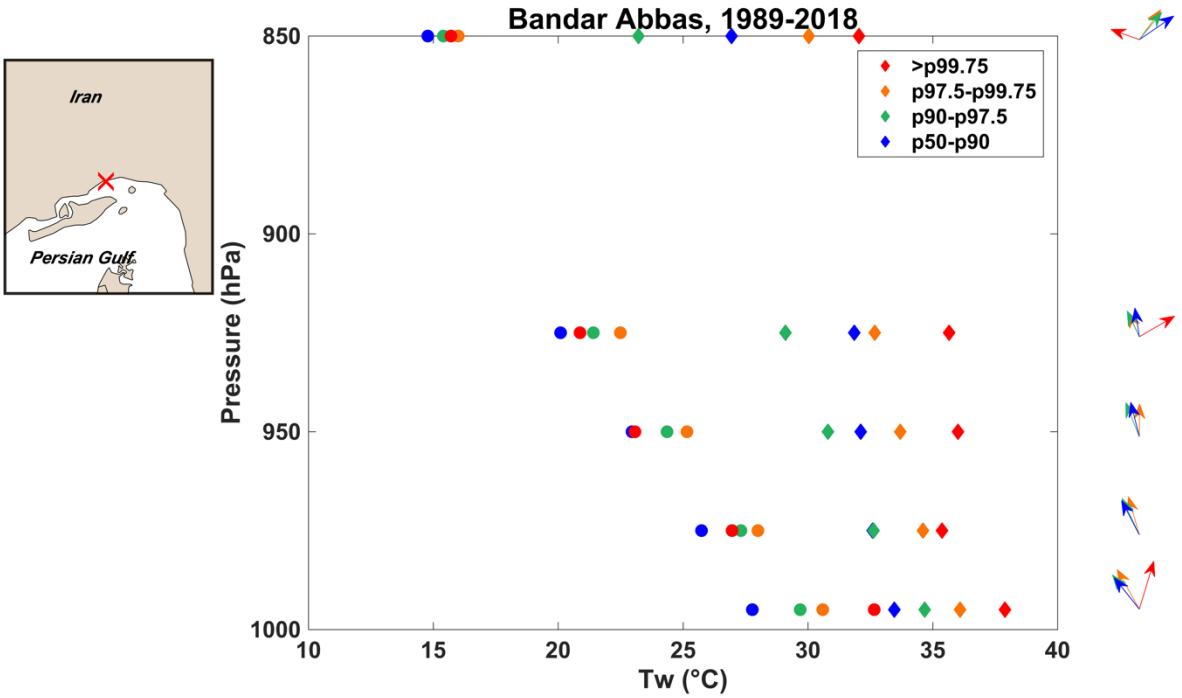

Figure S8. Vertical profiles of coastal extreme humid heat. Same as Figure S7 but for Bandar Abbas, Iran. Here, TW values greater than the annual 99.75th percentile comprise 5 days; those between the annual 97.5th and 99.75th percentiles, 42 days; those between the annual 90th and 97.5th percentiles, 139 days; and those between the annual 50th and 90th percentiles, 738 days.

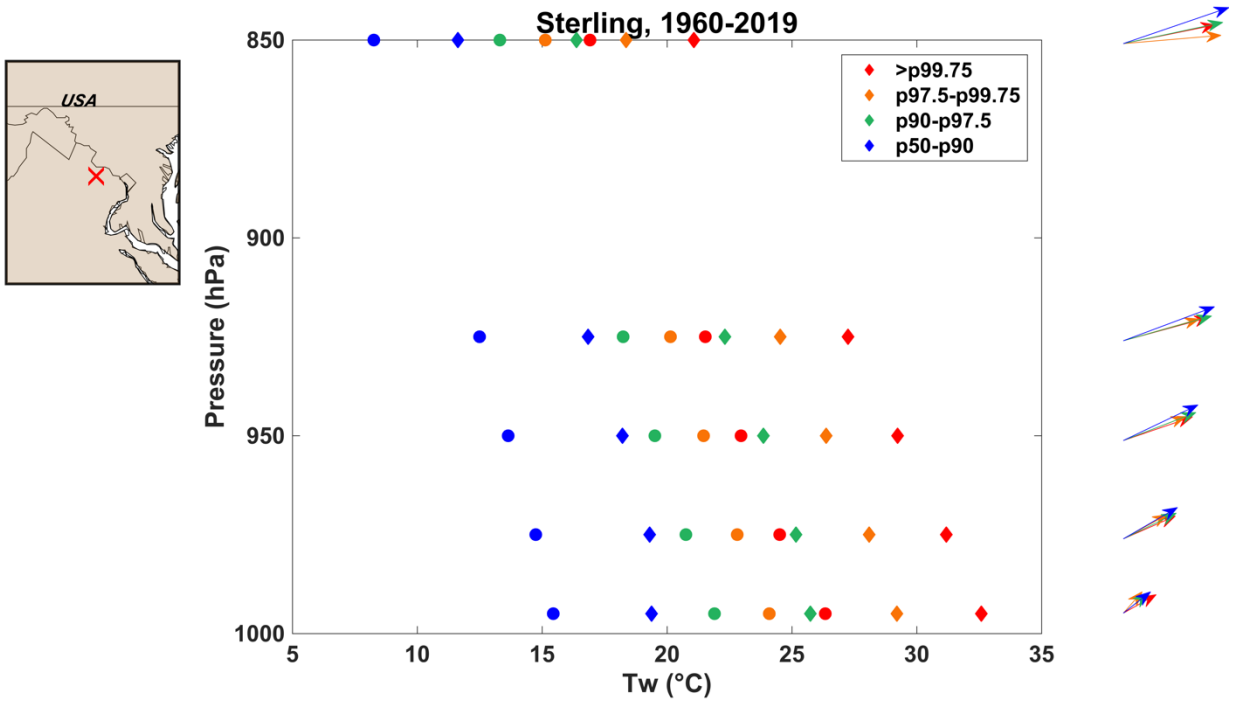

Figure S9. Vertical profiles of extreme humid heat in eastern North America. Same as Figure S8 but for Sterling, Virginia, USA. Here, TW values greater than the annual 99.75th percentile comprise 19 days; those between the annual 97.5th and 99.75th percentiles, 169 days; those between the annual 90th and 97.5th percentiles, 563 days; and those between the annual 50th and 90th percentiles, 3004 days.

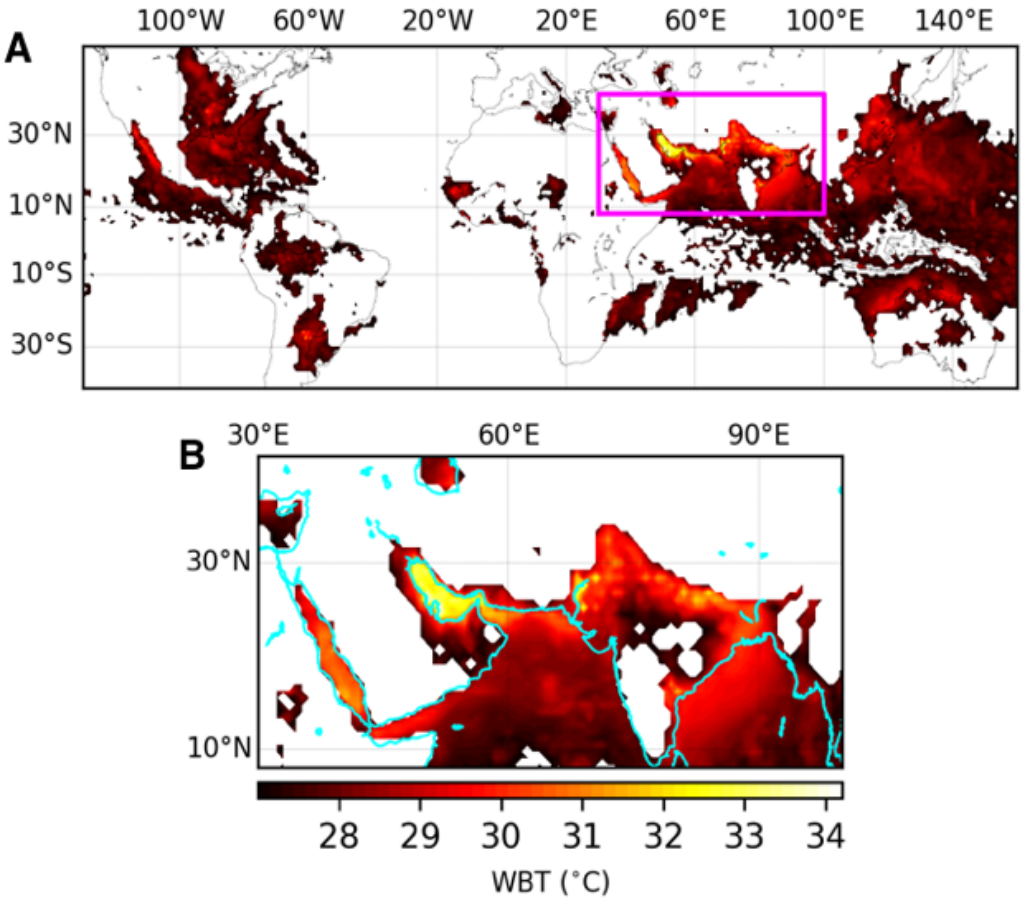

Figure S10. Highest observed extreme humid heat in reanalysis. (A) All-time maximum TW in the ERA-Interim (1979-2017). Values below 27°C are masked. (B) Zoomed-in perspective on the region with the highest TW values; the extent of this region is given by the magenta rectangle in (A).

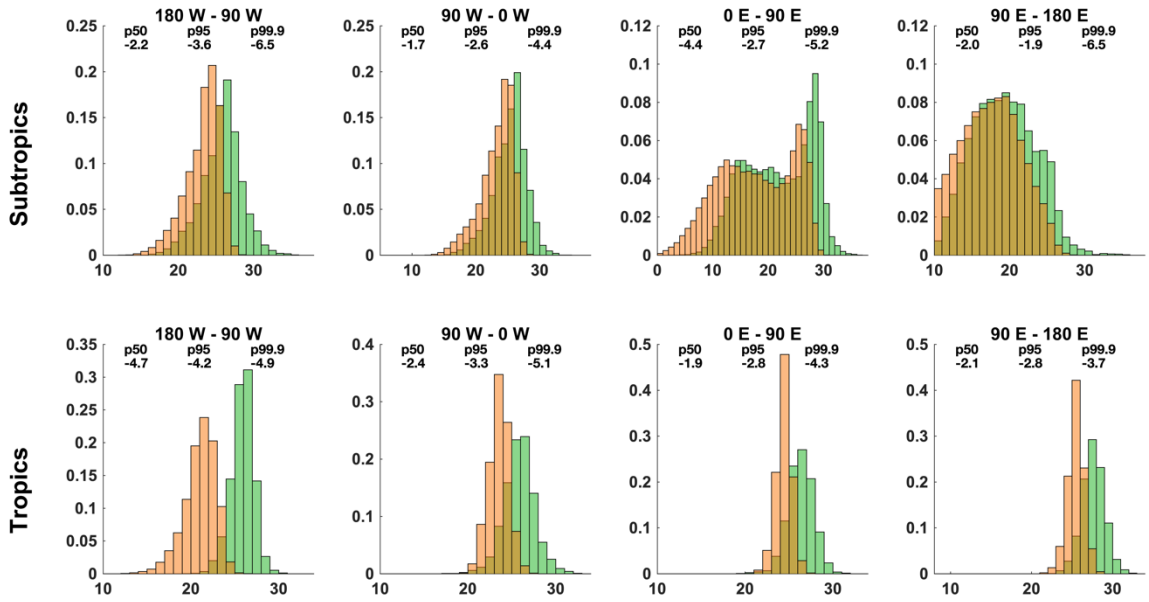

Figure S11. Distribution of ERA-Interim differences from weather stations across regions. Normalized frequency distributions of TW for the highest-TW stations in HadISD (green) and hottest grid cells in ERA-Interim (orange), where stations and grid cells are defined independently between the two datasets. Small type indicates biases in °C for the 50th, 95th, and 99.9th percentiles. Tropics (subtropics) are defined as 0°-15° (15°-35°) in each hemisphere; longitudinal bounds for each region are given in the titles of the subplots.

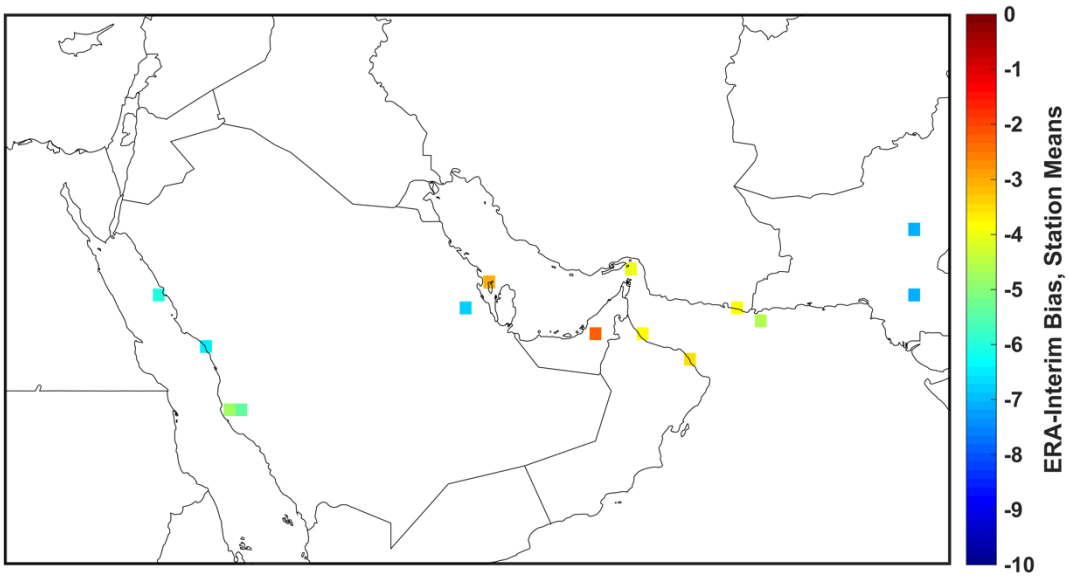

Figure S12. ERA-Interim differences from weather stations for extreme humid heat. Station-mean differences of ERA-Interim from weather stations, across all 33°C TW observations at the shaded HadISD stations. For each station, comparisons are made with the neighboring ERA-Interim grid cell with the highest TW value (regardless of precise distance), so as to minimize the penalty for ERA-Interim's spatial smoothing.

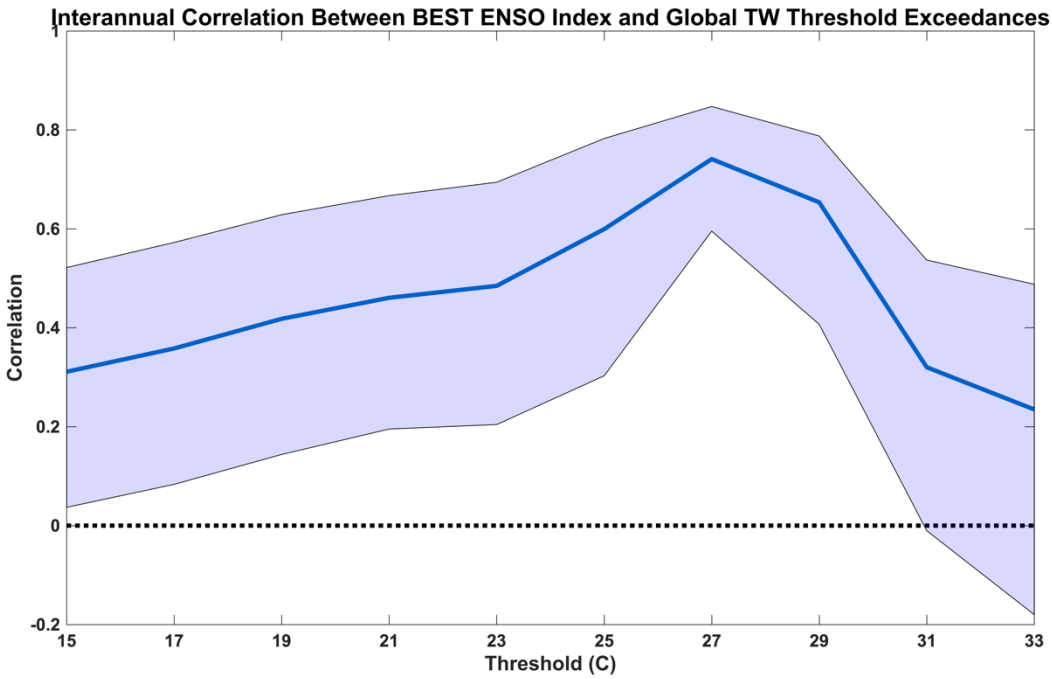

Figure S13. Correlation between ENSO and global extreme humid heat. Correlation between the Bivariate ENSO Timeseries [BEST] index and global counts of TW exceedances over 1979-2017. Shading shows the 5thand 95th percentile bounds based on 1000 bootstrapped samples of the timeseries for each threshold.

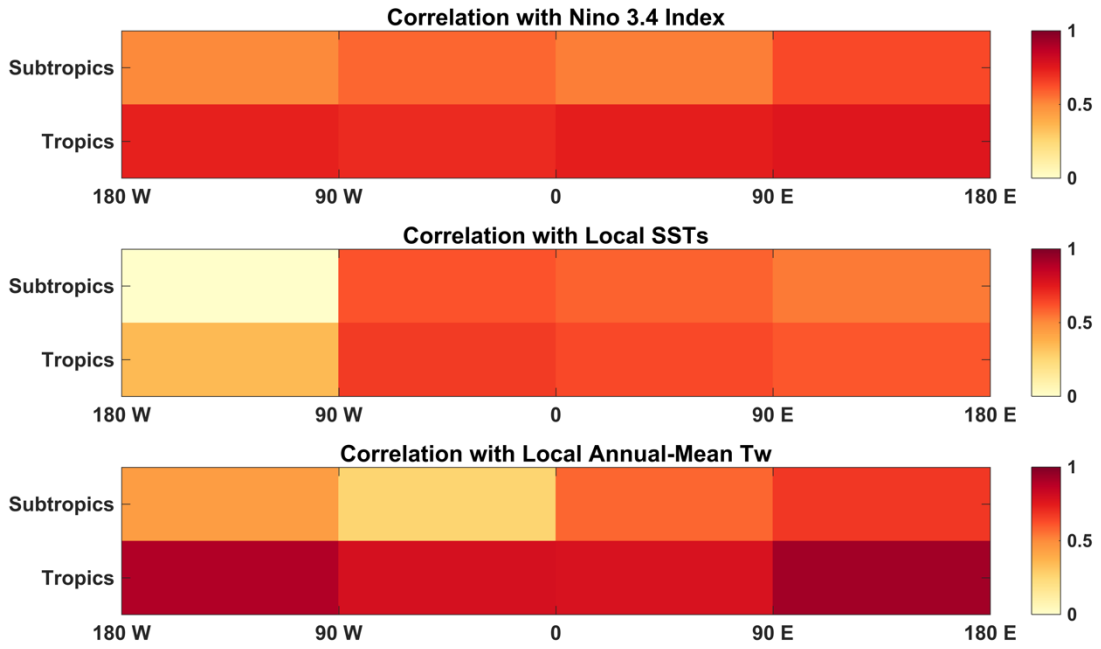

Figure S14. Correlations of extreme humid heat with major indices. Detrended correlation between regional annual station-days exceeding TW>=27°C and (top) DJF Nino 3.4 index; (middle) local JJA sea-surface temperatures from HadISST; and (bottom) local annual-mean TW from HadISD. Tropics (subtropics) are defined as 0°-15° (15°-35°) in each hemisphere.

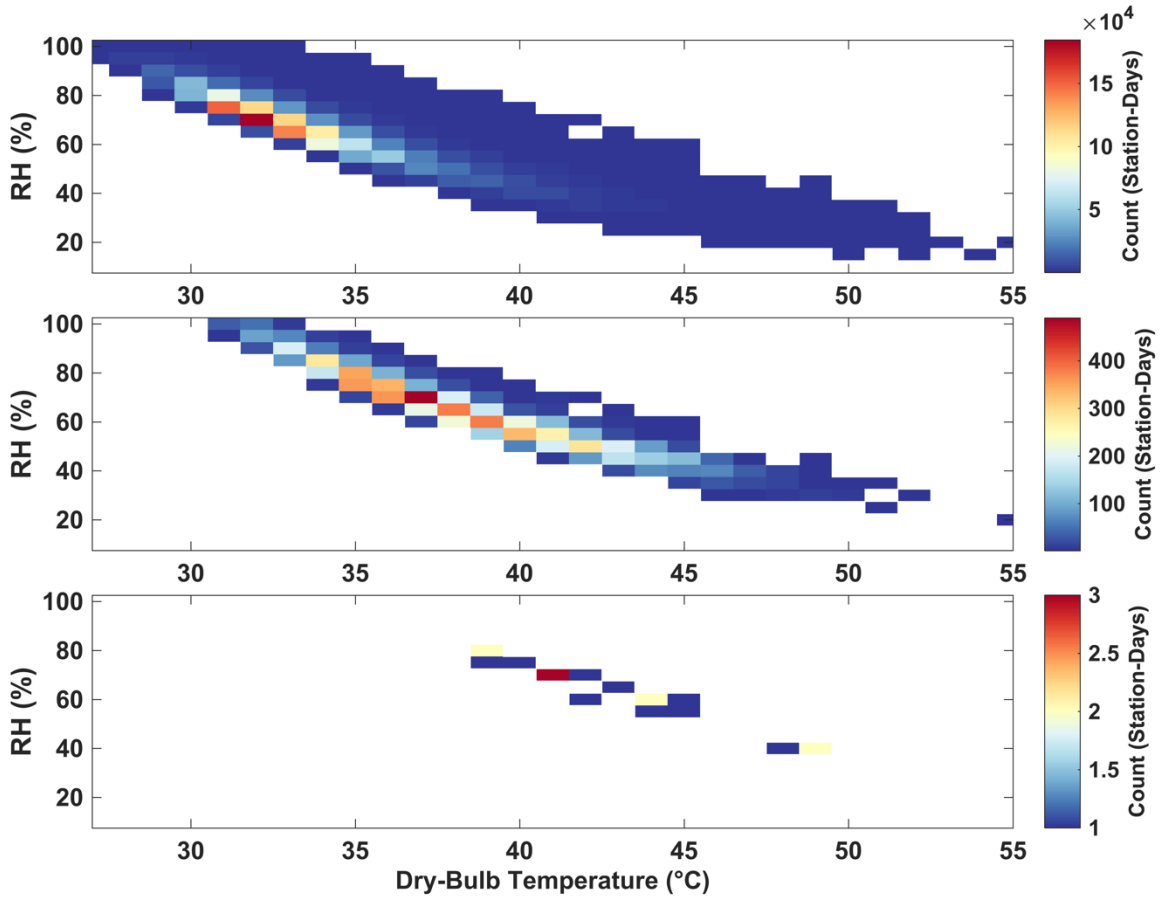

Figure S15. Temperature-humidity combinations leading to extreme humid heat. Frequency of dry-bulb temperature and relative humidity combinations associated with all occurrences of TW>=27°C (top), TW>=31°C (middle), and TW>=35°C (bottom) in HadISD.

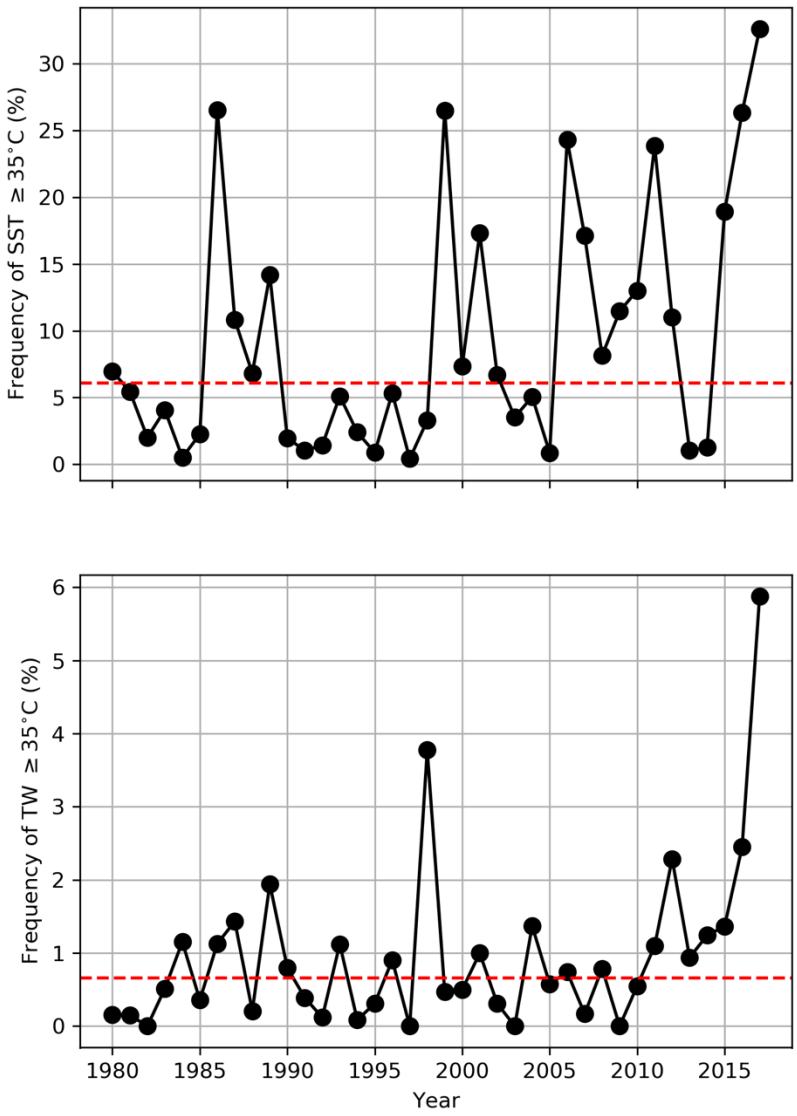

Figure S16. TW and SSTs >= 35°C in the Persian Gulf and Gulf of Oman. Top: Annual (July-September) percentage of ICOADS sea-surface temperature observations reported in the Persian Gulf or Gulf of Oman (23-31°N, 47-60°N) that exceed 35°C. Red line indicates the median. Bottom: Same as top but for percentage of TW observations exceeding 35°C.

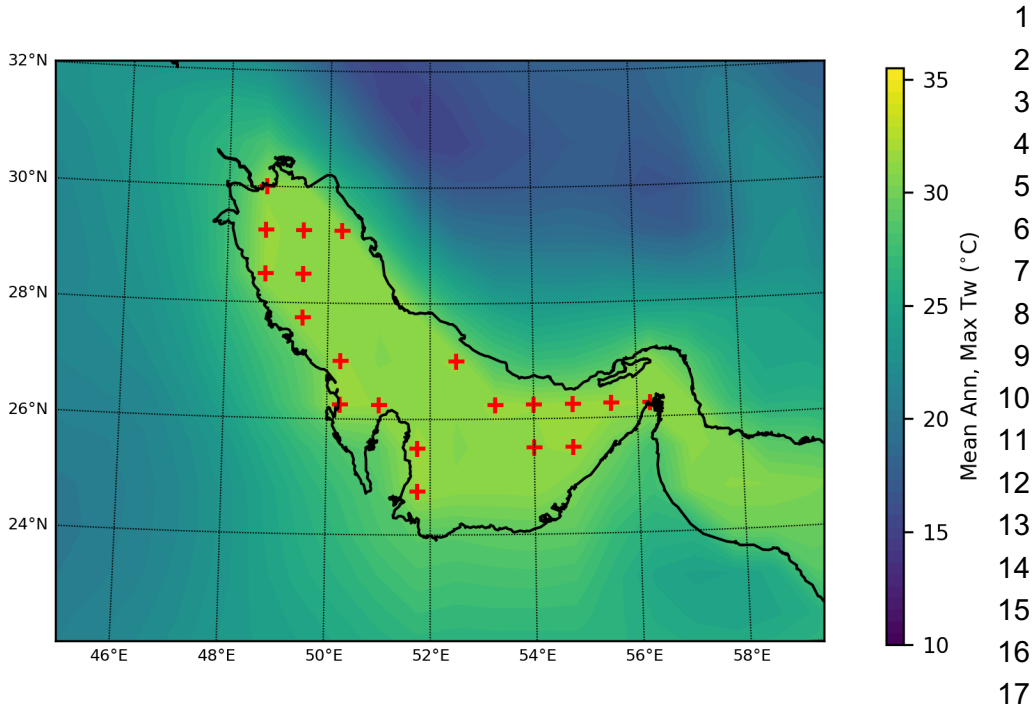

Figure S17. Mean annual-maximum TW in reanalysis. Mean annual-maximum near-surface TW over 1979-2017 according to the ERA-Interim reanalysis. Red crosses mark the 20 grid cells (land or ocean) with the highest values globally.

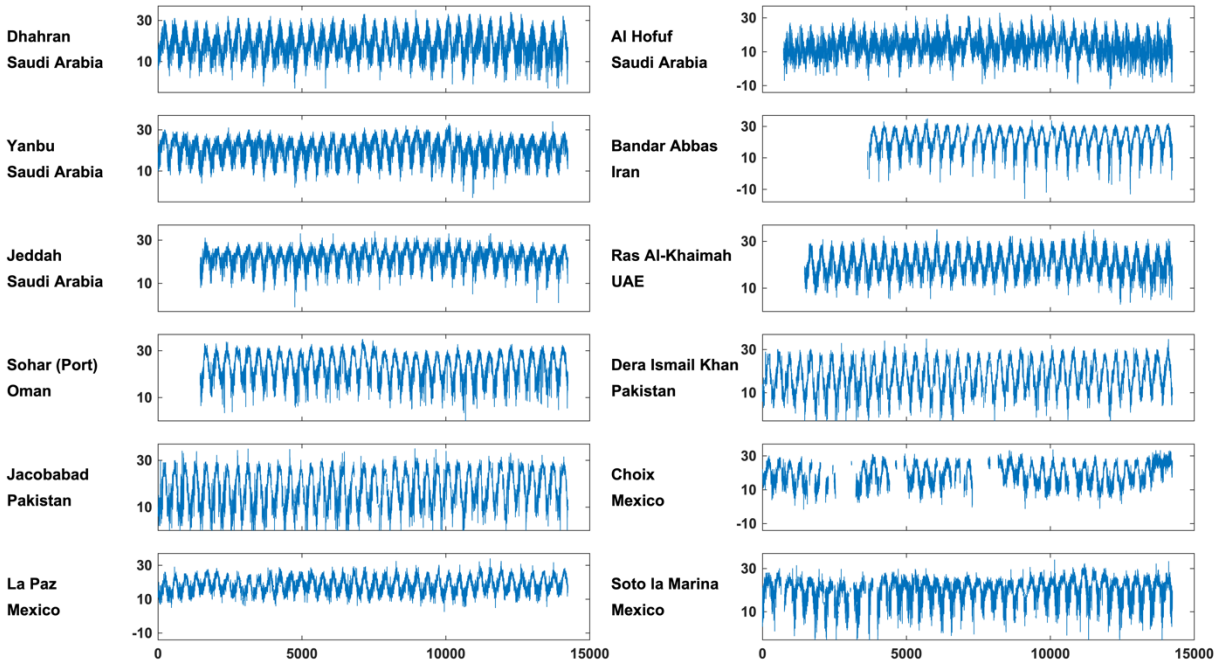

Figure S18. All dewpoints for selected extreme stations. Full timeseries (1979-2017) of daily-maximum dewpoint temperature for each station that has exceeded TW=33ºC at least 5 times. X-axis units are days since Jan 1, 1979.

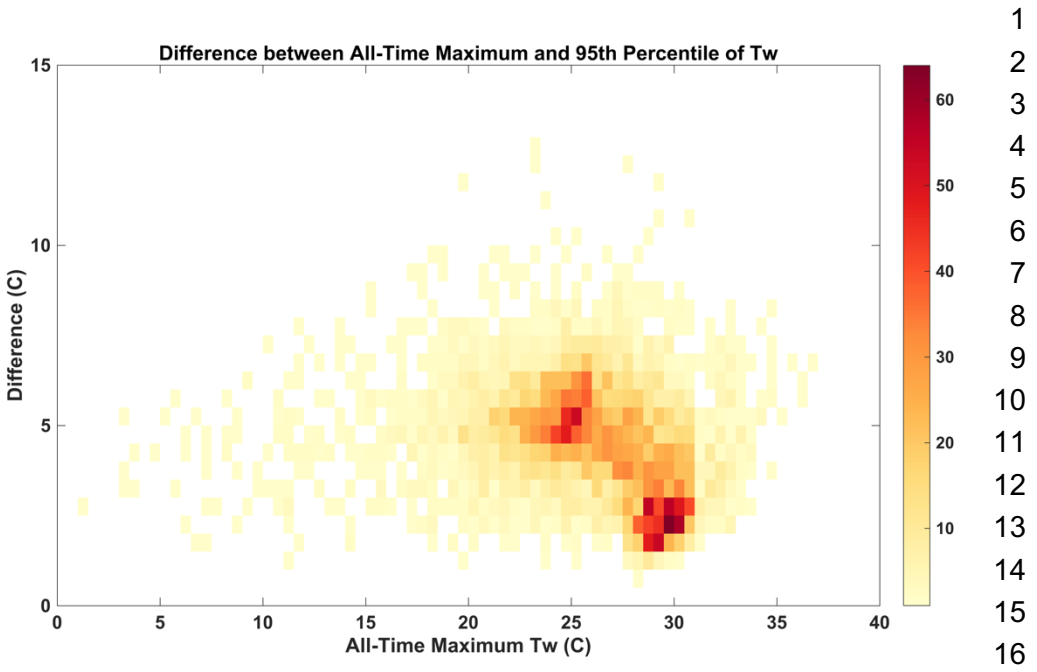

Figure S19. Extremity of TW all-time maxima. Heat map of differences between the all-time maximum TW at each station (c.f. Figure S1) and the overall 95th percentile of TW at the same station, with shading indicating the number of stations within a given 1ºC x 1ºC box. Two clusters are evident, representing typical tropical (lower right) and mid-latitude (upper left) climates. Differences are largest for mid-latitude locations, and decrease toward cold and warm extremes.

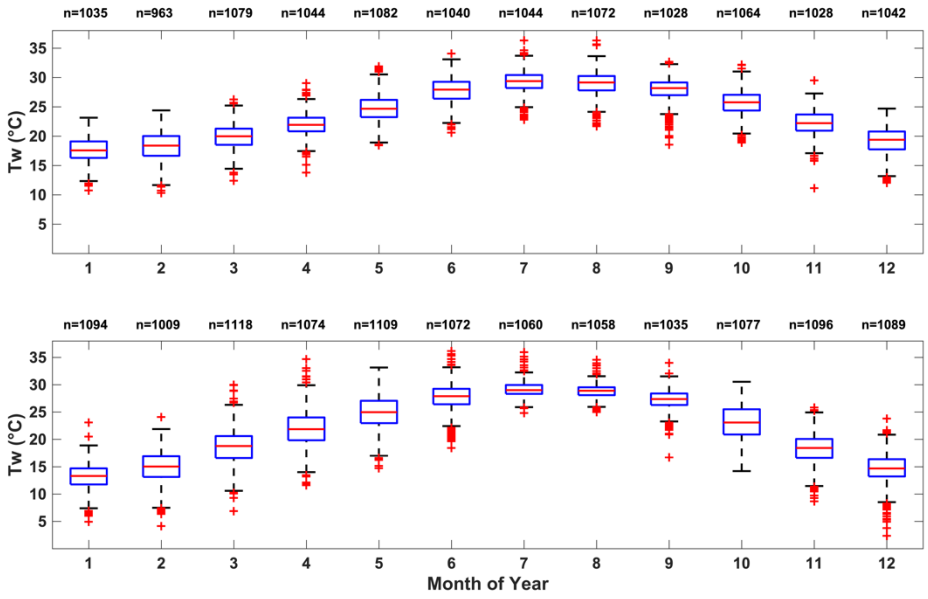

Figure S20. Annual patterns in TW on the Persian Gulf coast and in the Indus River Valley. Boxplots of daily-maximum TW, separated by month, for the two stations that have recorded TW=35ºC multiple times: Ras Al-Khaimah, UAE (top), and Jacobabad, Pakistan (bottom).

Table S1. Statistics for TW>=33°C stations. Details of all (*n=14)* stations that have recorded 3 or more days, over 3 or more different years, with a daily-maximum TW >= 33ºC. The 'years' column indicates the equivalent number of valid years of data available; pXX columns indicate the 99th, 90th, and 50th percentiles of daily-maximum TW over the entire station period of record; and in the final column, the distance from the coast is given, for stations situated near a marine coastline.

Lat	Lon	Location	Country	33+	First	Last	Years	p99	p90	p50	Region (Distance from Coast)
24.47	56.63	Sohar	Oman	69	1983	2017	34.4	32.5	30.7	25.7	Gulf of Oman coast (7.0 km)
28.28	68.45	Jacobabad	Pakistan	40	1981	2017	35.3	31.5	29.4	22.1	Indus River Valley
26.27	50.15	Dhahran	Saudi Arabia	26	2001	2017	38.0	32.0	28.3	21.7	Persian Gulf coast (6.5 km)
25.62	55.94	Ras Al-Khaimah	UAE	25	1988	2010	34.3	31.8	29.6	23.6	Persian Gulf coast (15.0 km)
31.91	70.90	Dera Ismail Khan	Pakistan	12	1980	2017	35.9	31.0	28.9	21.3	Indus River Valley
27.22	56.38	Bandar Abbas	Iran	10	1994	2017	27.6	31.9	30.5	24.7	Persian Gulf coast (3.0 km)
21.68	39.16	Jeddah	Saudi Arabia	8	1999	2010	33.6	30.7	28.5	25.0	Red Sea coast (7.0 km)
24.14	38.06	Yanbu	Saudi Arabia	8	2003	2006	38.1	31.3	28.5	24.2	Red Sea coast (7.5 km)
23.77	-98.20	Soto la Marina	Mexico	9	2006	2017	34.2	29.9	27.2	23.9	Gulf of Mexico coast (45 km)
24.17	-110.3	La Paz	Mexico	7	2001	2011	36.8	29.4	26.8	21.5	Gulf of California coast (1.0 km)
26.73	-108.28	Choix	Mexico	6	1993	2003	26.8	30.7	28.2	22.3	Gulf of California coast (100 km)
25.28	60.62	Chabahar	Iran	4	1992	2015	24.6	31.2	29.0	25.2	Persian Gulf coast (7.0 km)
25.29	49.49	Al Hofuf	Saudi Arabia	5	1993	2006	36.4	29.6	25.0	19.5	Persian Gulf coast (85 km)
26.27	50.63	Muharraq	Bahrain	3	1998	2001	33.3	31.9	29.6	23.5	Persian Gulf coast (2.5 km)

Table S2. Statistics for TW>=35°C stations. Same as Table S1 but for stations with any number of TW >= 35ºC occurrences.

Lat	Lon	Location	Country	35+	First	Last	Years	p99	p90	p50	Region (Distance from Coast)
28.28	68.45	Jacobabad	Pakistan	6	1987	2012	35.3	31.5	29.4	22.1	Indus River Valley
25.62	55.94	Ras Al-Khaimah	UAE	4	1995	2010	34.3	31.8	29.6	23.6	Persian Gulf coast (15.0 km)
21.68	39.16	Jeddah	Saudi Arabia	2	1999	2010	33.6	30.7	28.5	25.0	Red Sea coast (7.0 km)
31.91	70.90	Dera Ismail Khan	Pakistan	1	2017	2017	35.9	31.0	28.9	21.3	Indus River Valley
26.27	50.15	Dhahran	Saudi Arabia	1	2003	2003	38.0	32.0	28.3	21.7	Persian Gulf coast (6.5 km)

REFERENCES AND NOTES

1. P. E. Wheeler, The thermoregulatory advantages of hominid bipedalism in open equatorial environments: The contribution of increased convective heat loss and cutaneous evaporative cooling. *J. Hum. Evol.* **21,** 107–115 (1991).

2. M. Wehner, D. Stone, H. Krishnan, K. AchutaRao, F. Castillo, The deadly combination of heat and humidity in India and Pakistan in summer 2015. *Bull. Amer. Meteorol. Soc.*, **97,** S81–S86 (2016).

3. J.-M. Robine, S. L. K. Cheung, S. Le Roy, H. Van Oyen, C. Griffiths, J.-P. Michel, F. R. Herrmann, Death toll exceeded 70,000 in Europe during the summer of 2003. *C. R. Biol.* **331,** 171–178 (2008).

4. B. A. Revich, Heat-wave, air quality and mortality in European Russia in summer 2010: Preliminary assessment. *Ekol. Cheloveka Hum. Ecol.* 3–9 (2011).

5. T. K. R. Matthews, R. L. Wilby, C. Murphy, Communicating the deadly consequences of global warming for human heat stress. *Proc. Nat. Acad. Sci. U.S.A.* **114,** 3861–3866 (2017).

6. C. Mora, B. Dousset, I. R. Caldwell, F. E. Powell, R. C. Geronimo, C. R. Bielecki, C. W. W. Counsell, B. S. Dietrich, E. T. Johnston, L. V. Louis, M. P. Lucas, M. M. McKenzie, A. G. Shea, H. Tseng, T. W. Giambelluca, L. R. Leon, E. Hawkins, C. Trauernicht, Global risk of deadly heat. *Nat. Clim. Change* **7,** 501–506 (2017).

7. T. Kjellstrom, D. Briggs, C. Freyberg, B. Lemke, M. Otto, O. Hyatt, Heat, human performance, and occupational health: A key issue for the assessment of global climate change impacts. *Annu. Rev. Public Health* **37**, 97–112 (2016).

8. M. N. Sawka, C. B. Wenger, S. J. Montain, M. A. Kolka, B. Bettencourt, S. Flinn, J. Gardner, W. T. Matthew, M. Lovell, C. Scott, *Heat Stress Control and Heat Casualty Management* (US Army Research Institute of Environmental Medicine Technical Bulletin 507, 2003).

9. K. Parsons, Heat stress standard ISO 7243 and its global application. *Ind. Health*, **44**, 368–379 (2006).

10. S. C. Sherwood, M. Huber, An adaptability limit to climate change due to heat stress. *Proc. Natl. Acad. Sci. U.S.A.* **107**, 9552–9555 (2010).

11. C. Schär, Climate extremes: The worst heat waves to come. *Nat. Clim. Change* **6**, 128–129 (2016).

12. D. Lowe, K. L. Ebi, B. Forsberg, Heatwave early warning systems and adaptation advice to reduce human health consequences of heatwaves. *Int. J. Environ. Res. Public Health* **8**, 4623–4648 (2011).

13. E. G. Hanna, P. W. Tait, Limitations to thermoregulation and acclimatization challenge human adaptation to global warming. *Int. J. Environ. Res. Public Health* **12**, 8034–8074 (2015).

14. J. S. Pal, E. A. B. Eltahir, Future temperature in southwest Asia projected to exceed a threshold for human adaptability. *Nat. Clim. Change* **6**, 197–200 (2016).

15. E.-S. Im, J. S. Pal, E. A. B. Eltahir, Deadly heat waves projected in the densely populated agricultural regions of South Asia. *Sci. Adv.* **3**, e1603322 (2017).

16. E. D. Coffel, R. M. Horton, A. de Sherbinin, Temperature and humidity based projections of a rapid rise in global heat stress exposure during the 21st century. *Environ. Res. Lett.* **13**, 014001 (2018).

17. R. J. H. Dunn, K. M. Willett, D. E. Parker, L. Mitchell, Expanding HadISD: Quality-controlled, sub-daily station data from 1931. *Geosci. Instrum. Method. Data Syst.*, **5**, 473–491 (2016).

18. R. J. H. Dunn, K. M. Willett, P. W. Thorne, E. V. Woolley, I. Durre, A. Dai, D. E. Parker, R. S. Vose, HadISD: A quality-controlled global synoptic report database for selected variables at long-term stations from 1973-2011. *Clim. Past* **8**, 1649–1679 (2012).

19. D. P. Dee, S. M. Uppala, A. J. Simmons, P. Berrisford, P. Poli, S. Kobayashi, U. Andrae, M. A. Balmaseda, G. Balsamo, P. Bauer, P. Bechtold, A. C. M. Beljaars, L. van de Berg, J. Bidlot, N. Bormann, C. Delsol, R. Dragani, M. Fuentes, A. J. Geer, L. Haimberger, S. B. Healy, H. Hersbach, E. V. Hólm, L. Isaksen, P. Kållberg, M. Köhler, M. Matricardi, A. P. McNally, B. M. Monge-Sanz, J.-J. Morcrette, B.-K. Park, C. Peubey, P. de Rosnay, C. Tavolato, J.-N. Thépaut, F. Vitart, The ERA-Interim reanalysis: Configuration and performance of the data assimilation system. *Q. J. Roy. Meteorol. Soc.* **137**, 553–597 (2011).

20. N. A. Rayner, D. E. Parker, E. B. Horton, C. K. Folland, L. V. Alexander, D. P. Rowell, E. C. Kent, A. Kaplan, Global analyses of sea surface temperature, sea ice, and night marine air temperature since the late nineteenth century. *J. Geophys. Res.* **108**, 4407 (2003).

21. E. Freeman, S. D. Woodruff, S. J. Worley, S. J. Lubker, E. C. Kent, W. E. Angel, D. I. Berry, P. Brohan, R. Eastman, L. Gates, W. Gloeden, Z. Ji, J. Lawrimore, N. A. Rayner, G. Rosenhagen, S. R. Smith, ICOADS release 3.0: A major update to the historical marine climate record. *Int. J. Clim.* **37**, 2211–2232 (2016).

22. I. Durre, Y. Xungang, R. S. Vose, S. Applequist, J. Arnfield, *Integrated Global Radiosonde Archive (IGRA) Version 2*. (NOAA National Centers for Environmental Information, 2016).

23. N. S. Diffenbaugh, J. S. Pal, F. Giorgi, X. Gao, Heat stress intensification in the mediterranean climate change hotspot. *Geophys. Res. Lett.* **34,** L11706 (2007).

24. E. Byers, M. Gidden, D. Leclère, J. Balkovic, P. Burek, K. Ebi, P. Greve, D. Grey, P. Havlik, A. Hillers, N. Johnson, T. Kahil, V. Krey, S. Langan, N. Nakicenovic, R. Novak, M. Obersteiner, S. Pachauri, A. Palazzo, S. Parkinson, N. D. Rao, J. Rogelj, Y. Satoh, Y. Wada, B. Willaarts, K. Riahi, Global exposure and vulnerability to multi-sector development and climate change hotspots. *Environ. Res. Lett.* **13**, 055012 (2018).

25. T. Matthews, Humid heat and climate change. *Prog. Phys. Geog.* **42**, 391–405 (2018).

26. J. Sheffield, K. M. Andreadis, E. F. Wood, D. P. Lettenmaier, Global and continental drought in the second half of the twentieth century: Severity–Area–Duration analysis and temporal variability of large-scale events. *J. Climate* **22**, 1962–1981 (2009).

27. A. H. Sobel, I. M. Held, C. S. Bretherton, The ENSO signal in tropical tropospheric temperature. *J. Climate* **15**, 2702–2706 (2002).

28. C. Raymond, D. Singh, R. M. Horton, Spatiotemporal patterns and synoptics of extreme wet-bulb temperature in the contiguous United States. *J. Geophys. Res. Atmos.* **122**, 13,108–13,124 (2017).

29. A. Tetievsky, O. Cohen, L. Eli-Berchoer, G. Gerstenblith, M. D. Stern, I. Wapinski, N. Friedman, M. Horowitz, Physiological and molecular evidence of heat acclimation memory: A lesson from thermal responses and ischemic cross-tolerance in the heart. *Physiol. Genomics* **34**, 78–87 (2008).

30. L. Chapman, J. A. Azevedo, T. Prieto-Lopez, Urban heat and critical infrastructure networks: A viewpoint. *Urban Clim.* **3**, 7–12 (2013).

31. G. D. Bynum, K. B. Pandolf, W. H. Schuette, R. F. Goldman, D. E. Lees, J. Whang-Peng, E. R. Atkinson, J. M. Bull, Induced hyperthermia in sedated humans and the concept of critical thermal maximum. *Amer. J. Physiol.* **235**, R228-R236 (1978).

32. K. M. Willett, R. J. H. Dunn, P. W. Thorne, S. Bell, M. de Podesta, D. E. Parker, P. D. Jones, C. N. Williams Jr., HadISDH land surface multi-variable humidity and temperature record for climate monitoring. *Clim. Past* **10**, 1983–2006 (2014).

33. K. M. Willett, C. N. Williams Jr., R. J. H. Dunn, P. W. Thorne, S. Bell, M. de Podesta, P. D. Jones, D. E. Parker, HadISDH: An updateable land surface specific humidity product for climate monitoring. *Clim. Past* **9**, 657–677 (2013).

34. E. C. Mannshardt-Shamseldin, R. L. Smith, S. R. Sain, L. O. Mearns, D. Cooley, Downscaling extremes: A comparison of extreme value distributions in point-source and gridded precipitation data. *Ann. Appl. Stat.* **4**, 484–502 (2010).

35. G. J. Van Oldenborgh, M. Collins, J. Arblaster, J. H. Christensen, J. Marotzke, S. B. Power, M. Rummukainen, T. Zhou, Annex I: Atlas of global and regional climate projections. in *Climate Change 2013: The Physical Science Basis. Contribution of Working Group I to the Fifth Assessment Report of the Intergovernmental Panel on Climate Change*, T. F. Stocker, D. Qin, G.-k. Plattner, M. Tignor, S. K. Allen, Eds. (Cambridge Univ. Press, Cambridge, U.K, 2013).

36. J. Marsicek, B. N. Shuman, P. J. Bartlein, S. L. Shafer, S. Brewer, Reconciling divergent trends and millennial variations in Holocene temperatures. *Nature* **554**, 92–96 (2018).

37. J. R. Buzan, K. Oleson, M. Huber, Implementation and comparison of a suite of heat stress metrics within the community land model version 4.5. *Geosci. Model Dev.* **8**, 151–170 (2015).

38. R. Davies-Jones, An efficient and accurate method for computing the wet-bulb temperature along pseudoadiabats. *Mon. Wea. Rev.* **136**, 2764–2785 (2008).

39. I. Durre, R. S. Vose, D. B. Wuertz, Overview of the integrated global radiosonde archive. *J. Climate* **19**, 53–68 (2006).

40. C. P. Morice, J. J. Kennedy, N. A. Rayner, P. D. Jones, Quantifying uncertainties in global and regional temperature change using an ensemble of observational estimates: The HadCRUT4 data set. *J. Geophys. Res.* **117**, D08101 (2012).

41. Copernicus Climate Change Service (C3S) (2017): ERA5: Fifth generation of ECMWF atmospheric reanalyses of the global climate. Copernicus Climate Change Service Climate Data Store (CDS), https://cds.climate.copernicus.eu/cdsapp#!/home [accessed 10 November 2019]

42. I. Moradi, B. Soden, R. Ferraro, P. Arkin, H. Vömel, Assessing the quality of humidity measurements from global operational radiosonde sensors. *J. Geophys. Res. Atmos.* **118**, 8040–8053 (2013).

43. A. J. Simmons, K. M. Willett, P. D. Jones, P. W. Thorne, D. P. Dee, Low-frequency variations in surface atmospheric humidity, temperature, and precipitation: Inferences from reanalyses and monthly gridded observational data sets. *J. Geophys. Res.* **115**, D01110 (2010).

44. M. P. McCarthy, P. W. Thorne, H. A. Titchner, An analysis of tropospheric humidity trends from radiosondes. *J. Climate* **22**, 5820–5838 (2009).